Published in final edited form as:
Comput Med Imaging Graph. 2013 June ; 37(4): 272–280. doi:10.1016/j.compmedimag.2013.04.007.

Evaluation of optimized *b*-value sampling schemas for diffusion kurtosis imaging with an application to stroke patient data

Xu Yan[a], **Minxiong Zhou**[a], **Lingfang Ying**[a], **Dazhi Yin**[a], **Mingxia Fan**[a], **Guang Yang**[a], **Yongdi Zhou**[a], **Fan Song**[b], and **Dongrong Xu**[c,d,*]

[a]Key Laboratory of Brain Functional Genomics, Key Laboratory of Magnetic Resonance, Institute of Cognitive Neuroscience, East China Normal University, Shanghai 20062, China

[b]Department of Rehabilitation, Huashan Hospital of Fudan University, Shanghai 200040, China

[c]MRI Unit, Columbia University, Department of Psychiatry, NYSPI Unit 74, 1051 Riverside Drive, New York, NY 10032, USA

[d]New York State Psychiatric Institute, NYSPI Unit 74, 1051 Riverside Drive, New York, NY 10032, USA

Abstract

Diffusion kurtosis imaging (DKI) is a new method of magnetic resonance imaging (MRI) that provides non-Gaussian information that is not available in conventional diffusion tensor imaging (DTI). DKI requires data acquisition at multiple *b*-values for parameter estimation; this process is usually time-consuming. Therefore, fewer *b*-values are preferable to expedite acquisition. In this study, we carefully evaluated various acquisition schemas using different numbers and combinations of *b*-values. Acquisition schemas that sampled *b*-values that were distributed to two ends were optimized. Compared to conventional schemas using equally spaced *b*-values (ESB), optimized schemas require fewer *b*-values to minimize fitting errors in parameter estimation and may thus significantly reduce scanning time. Following a ranked list of optimized schemas resulted from the evaluation, we recommend the 3b schema based on its estimation accuracy and time efficiency, which needs data from only 3 *b*-values at 0, around 800 and around 2600 s/mm^2, respectively. Analyses using voxel-based analysis (VBA) and region-of-interest (ROI) analysis with human DKI datasets support the use of the optimized 3b (0, 1000, 2500 s/mm^2) DKI schema in practical clinical applications.

Keywords

Non-Gaussian diffusion; Diffusion kurtosis imaging; Diffusion tensor imaging; Optimized *b*-value; *b*-value sampling

1. Introduction

Diffusion tensor imaging (DTI) is a commonly used medical imaging method that characterizes the motion of water molecules in living tissues [1]. The DTI model is based on

*Corresponding author at: 1051 Riverside Drive, NYSPI Unit 74, New York, NY 10032, USA. Tel.: +1 212 543 5495; fax: +1 212 543 0522. dx2103@columbia.edu, drxudr@gmail.com.
maxwell4444@hotmail.com (X. Yan), zhoumin ecnu@163.com (M. Zhou), sullyying@126.com (L. Ying), yindazhi88@126.com (D. Yin), mxfan@phy.ecnu.edu.cn (M. Fan), gyang@phy.ecnu.edu.cn (G. Yang), yzhou12.yd@gmail.com (Y. Zhou), songfan@medmail.com.cn (F. Song).

the assumption that the random displacement of water molecules approximates the Gaussian distribution. However, due to the complexity of tissue structures, this assumption is not completely accurate; the non-Gaussian property should be considered, particularly at high *b*-values (e.g., larger than 1500 s/mm^2). The non-Gaussian effect is a result of many factors, such as cell structures, restricted intra- or extra-cellular compartments, permeability and water exchange [2]. Neglecting the non-Gaussian effect leads to inaccurate estimations of diffusion properties [3].

Recently, a new model called diffusion kurtosis imaging (DKI) [4] was proposed, which incorporates a nonlinear term into the mathematical expression of the displacement distribution to reflect the non-Gaussian property of diffusion. The conventional parameter, the apparent diffusion coefficient (ADC), and a new parameter called the apparent kurtosis coefficient (AKC) can be estimated simultaneously from this nonlinear diffusion function. The AKC value quantifies the amount of deviation from a Gaussian model; thus, it can provide some insight regarding the non-Gaussian property of biological tissues. These parameters can also be estimated using a tensor form [5–7]. In general, DKI is a more comprehensive model than DTI; it provides kurtosis information (AKC) in addition to conventional diffusion information (ADC) [2,3,8]. Recent studies using DKI have demonstrated that it provides improved sensitivity in detecting developmental and pathological changes in neural tissues compared to conventional DTI [9–14].

The DKI model is based on diffusion-weighted imaging (DWI) data that can be acquired using conventional pulse sequences for DTI. However, data must be acquired using at least 3 different *b*-values to estimate the nonlinear function embedded in the DKI model. In practice, a DKI acquisition schema typically uses more *b*-values to improve robustness and accuracy. In most cases, pulse sequences using 6 equally spaced *b*-values (ESB) (typically, *b*-values range from 0 to 2500 s/mm^2) are used in studies of the human brain [9–11]. Other studies have used 4 (0–2400 s/mm^2, 800 s/mm^2 incremental) [15] or even 41 *b*-values (0–4000 s/mm^2, 100 s/mm^2 incremental) [13]. Unfortunately, the efficiency of these sampling schemas is rarely carefully inspected or quantitatively compared.

Moreover, the common ESB schema (6 *b*-values: 5 non-zero + 1 baseline) usually takes over 10 min to cover the whole brain on a Siemens or Phillips MR scanner and almost twice that on a GE scanner (except for the latest GE 750 model, which was delivered only recently). To reduce scanning time, using fewer *b*-values is desired [15,16], as long as the accuracy of estimating parameters can be maintained. A new experimental design [17] was recently proposed to enhance precision, which optimizes the configuration of both the distribution of gradient directions and the *b*-values by minimizing the Cramér–Rao lower bound of the DKI parameters. While it is prohibitively complicated in theory, and optimizing these configurations requires modification of the pulse sequence; most investigators do not have easy access to this method. Considering the time required for data acquisition and processing, Jensen and his colleagues empirically suggested the use of 3 *b*-values in clinical studies to avoid modifying the pulse sequence [16]. These investigators demonstrated this technique in visual and region-of-interest (ROI) examinations of one volunteer. Although, this method may be valuable, it must be quantitatively evaluated and validated in terms of its accuracy and efficiency. Therefore, it has not yet been widely accepted by the neuroimaging community.

We provide an assessment on the effectiveness of various DKI schemas and search for the optimal combinations of *b*-values by testing exhaustively every possible permutation using data from multiple *b*-values. Our finding is that those optimal DKI schemas usually contain data acquired at *b*-values that are not equally distributed. Such schemas can achieve comparable accuracy that the conventional acquisition schemas may achieve, however, with

fewer *b*-values but requiring less than half of the acquisition time. Based on a list of optimized schemas resulted from performance evaluation, we recommend the 3b schema due to its estimation accuracy and time efficiency, which needs data from only 3 *b*-values at 0, around 800 and around 2600 s/mm^2, respectively. Examining the performance of the optimized and conventional acquisition schemas using data collected from stroke patients have verified our findings.

2. Materials

2.1. Datasets of 12 b-values

After 5 healthy volunteers provided written consent, their DKI data were collected using a 3T Siemens Trio system at East China Normal University. This study was approved by the Institutional Ethics Committee of East China Normal University. Each dataset contained one baseline image (*b*-value = 0) and 11 DW images at non-zero *b*-values (12 *b*-values in total) along every gradient direction. The diffusion gradient was applied in 12 non-collinear directions. The non-zero *b*-values ranged from 600 to 2600 s/mm^2 in 200 s/mm^2 increments. The range of *b*-values used was similar to that recommended by previous reports [4,6]. All DWI data were acquired with a number of excitation (NEX) = 2 (2 averages). To suppress noise contributing to the DKI model estimation, we acquired 8 extra sets of baseline data (thus, a total of 10 baseline images were used in each dataset).

The other imaging parameters were as follows: TR = 5300 ms (3 subjects) or 6100 ms (2 subjects), TE = 110 ms, matrix = 128 × 128, FOV = 256 mm × 256 mm (4 subjects) or 230 mm × 230 mm (1 subject), slice thickness = 3 mm with no gap. There were slight differences in the images protocols used for each of the 5 volunteers, such as in TR and FOV values, because these datasets were collected during the time we were testing to define the most effective imaging protocol. We did not attempt to rescan participants because we believe that the variance between datasets could better serve our purpose for evaluating the different acquisition schemas used.

2.2. Stroke patient datasets

DKI datasets from 17 left-hemispheric stroke patients (age 46–76, mean age 62 ± 8, 13 male, with pure motor deficits from a subcortical stroke that occurred in the left motor pathway) and 19 healthy controls (age 45–76, mean age 59 ± 9, 10 male) were collected using a 3T Siemens Trio system at East China Normal University after each participant gave their written consent. This study was approved by the Institutional Ethics Committee of East China Normal University. Patients were selected from the outpatient and inpatient services at Huashan Hospital, which is affiliated with Fudan University in Shanghai, China. DWI data were acquired at 6 *b*-values (equally spaced with 0–2500 s/mm^2) with NEX = 2. We used 12 non-collinear directions of diffusion gradient. The other imaging parameters were as follows: TR = 5300 ms, TE = 110 ms, matrix = 128 × 128, FOV = 256 mm × 256 mm, slice thickness = 3 mm with no gap.

3. Methods

We will first present the processing procedure used for DKI data and then elaborate on the experimental design used to test the efficiency of the various acquisition schemas for the datasets at 12 *b*-values. Once the optimized acquisition schema is identified by the experiment, we describe a plan to validate its effectiveness versus the conventional ESB schemas via application to data from stroke patients.

3.1. Processing DKI data

All DWI data were routinely smoothed using a 3D Gaussian Kernel with *a full width at half maximum* (FWHM) of 3 mm [9,10,18]. Next, we corrected distortion in the DWI data induced by the eddy current using "eddy correct" and removed any non-brain area with "BET" toolbox in FSL (http://www.fmrib.ox.ac.uk/fsl/). We thus obtained a brain mask. We then averaged the ten baseline images and two repetitions of the DWI images, which were already corrected for distortion. Finally, we calculated ADC and AKC maps along each gradient direction and computed the mean diffusion (MD) and mean kurtosis (MK) by averaging all of the ADC and AKC along each direction. For DWI datasets with more than 2 nonzero *b*-values, we estimated ADC and AKC values based on the following nonlinear equation:

$$\frac{S(b)}{S(0)}=\exp\left(-bD+\frac{1}{6}\times b^2D^2K\right) \quad (1)$$

where b is the b-value, D and K denote the ADC and AKC value, $S(0)$ and $S(b)$ denote the baseline and DWI measurement at a certain b-value. For DWI datasets acquired at only 2 nonzero b-values, we calculated their ADC and AKC by solving the following equation directly [16]:

$$\begin{cases} \widehat{D}=(b_2D_1-b_1D_2)/(b_2-b_1) \\ \widehat{K}=6(D_1-D_2)/(b_2-b_1)\,\widehat{D}^2 \end{cases} \quad (2)$$

where b_1 and b_2 are 2 nonzero b-values. D_1 and D_2 are diffusion coefficients calculated by their individual DWI data at the corresponding b-value:

$$D_n=\frac{\ln S(b_n)/S(0)}{b_n}\ (n=1,2) \quad (3)$$

Following recommendations found in the literature [18], we applied the same physical and biological constraints to ADC and AKC in that both should be non-negative values. These algorithms were implemented in MATLAB (http://www.mathworks.com).

3.2. Analyzing data collected at 12 b-values

In this subsection, we report the comparisons that were conducted between the various b-value sampling schemas based on the data collected at 12 b-values. We also describe how we searched for the optimized sampling schemas.

3.2.1. Exhaustive test—We compared all possible acquisition schemas by exhausting the possible number of b-values and permutations of b-values. First, we constructed a series of new DKI datasets by extracting subsets of data from the existing datasets collected at 12 b-values. In particular, we created these datasets using one baseline image plus DWI data collected at 5, 4, 3 or 2 non-zero b-values (in short 6b, 5b, 4b and 3b, respectively). Thus, each permutation yields a potential acquisition schema. We tested all of these potential schemas against the ESB schema to seek the optimized schemas.

To compare performances of these schemas, we estimated ADC and AKC maps (parameter maps) from these datasets. We took those parameter maps estimated using the complete dataset of 12 b-values as the "ground truth". We then used root mean square error (RMSE) to quantify the differences of the resulting ADC and AKC maps between the designated schema and the ground truth:

$$\mathrm{RMSE}=\sqrt{\frac{1}{N}\sum_{n=1}^{N}\sum_{x\in\Omega}\left(I_n\left(x\right)-U_n\left(x\right)\right)^2} \quad (4)$$

where Ω is the set of voxels within the brain mask calculated previously (Section 3.1), n denotes a certain gradient direction of DWI dataset and N is the total number of the gradient directions. I_n and U_n denote either ADC or AKC parameter maps along the nth gradient direction and its corresponding ground truth, respectively.

We calculated the RMSE for all possible acquisition schemas using 3b, 4b, 5b and 6b and ranked them according to their RMSE values. We recorded the highest 10 ranked schemas for each of the 5 participants and denoted them as *high-performance* schemas. To evaluate the impact factor of each *b*-value on the performance of the acquisition schemas, we calculated the probability of each *b*-value occurring in the 50 recorded schemas. Note that statistics analyses for each *b*-value were performed separately for schemas using 3b, 4b, 5b and 6b. Therefore, 50 high-performance schemas for each of the 4 *b*-value cases across all 5 participants were obtained. Consequently, this analysis yielded 4 distributions of occurrence probabilities of *b*-values in each of the 4 *b*-value cases.

Finally, for each *b*-value case (3b, 4b, 5b and 6b, respectively), we averaged the ranking of each schema (based on RMSE of parameter map) across all 5 participants so that each schema received an average ranking index. This process is supposed to statistically eliminate bias that could have been contained in individual participant and this index was readily to be used for identifying the best schema (denoted as the optimized, or OPT). For example, if a schema ranked 1, 2, 3, 4, and 5, respectively, for the 5 participants, its average ranking would be 3. Again, optimized schema identification was completed for each of the 4 *b*-value cases separately because the acquisition time for these schema cases differ.

3.2.2. Visual test—We also visually compared the MD and MK maps generated by the conventional ESB and optimized schemas. We wanted to examine the relationships between the accuracy of the estimations of the parameter maps and the number of *b*-values involved in generating each. By comparing the results against the ground truth, we aimed to identify differences that various schemas differentiated from the standard approach in performance.

3.2.3. Region-of-interest (ROI) test—In addition, we conducted a ROI test to compare the OPT and ESB schemas. For each participant, an ROI was manually drawn in regions identified as sensitive to different schema according to the visual test, and mean MD and MK values in the ROI were calculated. We then estimated and compared the errors, which was defined as the absolute difference between the mean MD, MK values and their corresponding ground truth.

3.3. Stroke data

In this section, we validated the results of our experiments using data collected at 12 *b*-values (Section 3.2) in terms of the optimized schema's effectiveness using real human data. We used the DKI data from a study of stoke patients to evaluate the performance of one optimized acquisition schema that uses 3 *b*-values (and thus requires the least acquisition time) against the conventional ESB schema that uses 6 *b*-values. For this purpose, we used voxel-based analysis and region-of-interest analysis to examine the resulting DKI parameters of these two schemas. These analyses are commonly used in clinical studies.

The original DKI dataset was collected using an ESB schema containing 6 *b*-values, namely, $b = 0$, 500, 1000, 1500, 2000 and 2500 s/mm^2 (acquisition time = 10 min 47 s). We did not

reattempt data acquisition using the optimized DKI schemas; instead, we constructed new datasets using the DKI data collected at 6 *b*-values. The optimized schema we used for this test was supported by our exhaustive test in Section 3.2 (Table 1). The new datasets contained data collected at 3 *b*-values ($b = 0$, 1000, 2500 s/mm^2, acquisition time = 4 min 25 s). We estimated MD and MK in order to conduct these evaluations.

3.3.1. Voxel-based analysis (VBA)—We used SPM8 (http://www.fil.ion.ucl.ac.uk/spm/) to make group comparisons of VBA on the MD and MK maps between the stroke and control groups. First, we normalized all of the baseline images collected from each participant to the standard EPI template provided by SPM8. The resulting deformation fields were applied to normalize their corresponding MD and MK maps to the template space. We then smoothed these normalized maps using a Gaussian kernel with an 8 mm FWHM. Finally, we performed a two-sample *t*-test on the smoothed MD and MK maps in the template space to compare the 19 healthy controls to the 17 stroke patients. Voxels with $P < 0.00001$ (uncorrected) and cluster size > 100 voxels were considered to show a statistically significant difference between the two groups.

3.3.2. Region-of-interest (ROI) analysis—We used ROI analysis to study the performance of the two acquisition schemas by comparing the individual MD and MK maps for all 36 participants (19 controls and 17 stroke patients) in the study. Two ROIs in the corona radiata and brainstem, which are the most commonly studied regions in stroke patients, were manually drawn on the averaged MK maps (averaging of the normalized MK maps of all participants) by one experienced investigator who is an expert in neuroanatomy. The mean MD and MK values in these ROIs were calculated for each participant.

4. Results

4.1. Data of 12 b-values

In the exhaustive test, we sorted all combinations of *b*-values based on the RMSE values of the parameter maps and calculated the occurrence probability of each *b*-value in the top 10 combinations. The results clearly showed that each *b*-value contributed unequally to minimizing the error in the estimation (Fig. 1). In the high-performance schemas (the top 10 schemas for each participant) of all 3b to 6b cases, the *b*-values at the two ends of the *b*-value range (600–1200 and 2400–2600 s/mm^2) had significantly higher occurrence probabilities than those in the middle range of *b*-values, especially those between 1600 and 2000 s/mm^2 (Fig. 1).

We were thus able to identify the optimized schemas (i.e., the one of the best average ranking) for 3b to 6b cases, and to compare them with the ESB schemas (Table 1). The average ranking of these 4 optimized schemas, namely, OPT 3b, 4b, 5b and 6b schemas, were 1.0, 1.2, 1.0, and 1.2, respectively. Similarly, the *b*-values of these optimized schemas were all located at the two end positions of the range, i.e., 600–1200 and 2400–2600 s/mm^2. On one hand, the RMSE of the ADC and AKC in the optimized schemas were much lower than those in the ESB schemas in all 3b to 6b cases (this difference is especially pronounced in the 3b case). On the other hand, as the number of *b*-values involved in the schemas decreased, the RMSE of the ADC and AKC increased in both the ESB and optimized schemas; the increased ratios of the optimized schemas were lower than those of the ESB schemas. Generally, the optimized schemas outperformed the conventional schemas either with more or fewer *b*-values.

Statistical analyses of the performance of the 5 types of schemas, including the high-performance case and the other 3b to 6b cases, were conducted by bootstrapping the exhaustive test of all of the *b*-values cases. The high-performance schemas that analyzed

here satisfied the two-ends *b*-values criterion identified via the above statistical procedure, which was not limited to the top 10 schemas. The results showed that the high-performance schemas generated RMSEs within a narrow region of the lower end of RMSE value range (0.07 ± 0.03 for MD and 0.14 ± 0.04 for MK), whereas the 3b to 6b cases generally yielded higher and more widely distributed RMSE errors (Fig. 2).

In the visual comparison, we only needed to examine the MD and MK maps of the 6b and 3b cases because we knew that the estimation accuracy of the parameter maps decreased slowly as the number of *b*-values decreased. We found that MD and MK maps that were estimated from the optimized datasets were consistent to the ground truth of both the 6b and 3b cases (Figs. 3 and 4). For ESB schemas, the quality of the MK map was maintained in the 6b case; however, the quality of the MK map clearly decreased in the 3b case, in which there were noticeable image artifacts (Figs. 3 and 5).

In the ROI test, ESB 3b schemas performed worst (generated generally higher estimation error than did the OPT 6b and ESB 6b schemas), while the estimation errors of the OPT 3b schemas were similar to those of the 6b schemas (Fig. 6).

4.2. Stroke patient data

The VBA results of the study involving stroke patients revealed that the OPT 3b schema performed similarly to the conventional ESB 6b schema for both the MD and MK maps. The resulting statistics of the parametric maps were well matched, except for some minor regions (Fig. 7). Significant differences in the MD and MK values between the stroke and control groups were detected; this was observed mainly in the corticospinal tract of the left hemisphere, as well as the right hemisphere (with much smaller cluster size). These two schemas yielded similar statistical data including cluster sizes, peak *t*-values, and their corresponding coordinates as defined in the Montreal Neurological Institute (MNI) template space (Table 2).

The ROI analysis demonstrated that the two acquisition schemas produced similar MD and MK values for each of the 36 participants in the stroke study (Fig. 8), with a mean difference of 0.0088 ± 0.0056 μm^2/ms (MD), 0.03557 ± 0.0105 (MK) in ROI 1 and 0.0072 ± 0.0135 μm^2/ms (MD), 0.0431 ± 0.0157 (MK) in ROI 2.

5. Discussion

Previously published studies involving the DKI model have used various acquisition schemas to obtain DKI data. The schema using one baseline and 5 non-zero *b*-values was considered sufficient for parameter estimation [4–6,9]. Although using fewer *b*-values is desired to reduce acquisition time, doing so was thought to compromise the accuracy of parameter estimation [5]. However, the performance of these acquisition schemas has not been quantitatively studied. In this work, we quantitatively and systematically evaluated the estimation accuracy of all possible acquisition schemas using DKI data collected at 12 *b*-values. We have demonstrated a potential method to optimize the acquisition schema of the DKI model and showed changes in its accuracy related to the number of *b*-values used. We were subsequently able to identify 4 optimized DKI schemas using different numbers of *b*-values, namely OPT 3b to 6b schemas (Table 1). Among these optimized schemas, we recommend the OPT 3b schema due to its time efficiency; this schema requires only one baseline image as well as DWI data collected at one low and one high *b*-value.

Our work supports Jensen and his colleagues [8]; the acquisition process can be accelerated by reducing the number of *b*-values, but the combination of *b*-values should be carefully considered to minimize estimation error. In our exhaustive test, we found that datasets can

generate more robust and accurate estimation results using optimized acquisition schemas when compared to using conventional ESB schemas (Fig. 1). Compared to the conventional acquisition schema (ESB 6b schema), optimized schemas can achieve similar accuracy with fewer *b*-values, and may save more than half of the acquisition time. Our experiment using stroke patient data validated this finding. The VBA and ROI analysis demonstrated that DKI datasets using the OPT 3b schema (Table 1) may perform comparably well with those using an ESB 6b schema (Figs. 7 and 8).

We believe that two main reasons account for the non-uniform distribution of *b*-values in the optimized acquisition schemas. First, the distribution of water molecules is dominantly Gaussian at low *b*-values and attenuation of the DWI signal is mainly caused by the first order term of ADC. Thus, using data with low *b*-values ensures highly accurate ADC estimations. Second, diffusion properties related to non-Gaussian factors become more significant as the *b*-value increases, especially when the *b*-value is higher than 2000 s/mm^2. Because the AKC value represents deviation from a Gaussian model of water motion, using more DWI data collected at high *b*-values between 2000 and 3000 s/mm^2 (generally accepted as the proper range of maximum *b*-values for DKI [8]) is supposed to make AKC estimates more robust. Therefore, DKI schemas composed of DWI data acquired at the two ends of the generally accepted range of *b*-values are capable of producing ADC and AKC simultaneously with greater accuracy.

Based on our experiment, we believe that reducing DKI acquisition time in clinical studies by reducing the number of *b*-values is feasible. By using the OPT 3b schema, we can reduce the acquisition time to only 4 min 25 s (12 gradient direction, NEX = 2) or 5 min 23 s (30 gradient direction, NEX = 1) on a Siemens scanner, which is much faster when compared to the conventional ESB 6b schemas (approximately 10 min acquisition time) and may greatly facilitate clinical applications of DKI in practice.

Acknowledgments

This paper is supported in part by a Grant from Shanghai Commission of Science and Technology (Grant# 10440710200), China; a Grant from the Fostering Program of a China National Nature Science Foundation Key Project (Approval # 91232701); a Grant from the 12th Five-year Plan Supporting Project of the Ministry of Science and Technology of the People's Republic of China (Grant# 2013BAI10B03); a Grant from the Large Instruments Open Foundation of East China Normal University, and in part by an NIH/NIMH Grant P50 MH090966-01, and an NIBIB Grant 1R03EB008235-01A1.

Biography

Xu Yan is a Ph.D. candidate in the Department of Physics, East China Normal University. His research interest includes post-processing and analysis methods for diffusion imaging and other MRI based techniques.

MinXiong Zhou is a Ph.D. candidate in the Department of Physics, East China Normal University. Her research interest focuses on MR image processing.

Lingfang Ying is a Master candidate in the Institute for Advanced Studies, East China Normal University. Her research interest focuses on data analysis and clinical applications of diffusion imaging.

Dazhi Yin is a Ph.D. candidate in the Department of Physics, East China Normal University. His research interest focuses on MR images processing and its applications in medicine.

Mingxia Fan, M.D. is an associate professor in Shanghai Key Laboratory of Magnetic Resonance, East China Normal University. Her research interest focuses on biological and clinical applications of advanced MRI techniques.

Guang Yang received his Ph.D. from Department of Physics, East China Normal University. Now he is an associate professor in Shanghai Key Laboratory of Magnetic Resonance, East China Normal University. His research interest includes MRI image processing and experiments simulation.

Yongdi Zhou obtained his Ph.D. in neuroscience from University of California, Los Angeles, now is a professor of psychology, East China Normal University. His research interest focuses on the cognitive neuroscience and neurophysiology.

Fan Song, M.D. is working at Department of Rehabilitation Medicine, Huashan Hospital, Fudan University. Her research interest focuses on investigation of stroke rehabilitation using functional MRI.

Dongrong Xu obtained his Ph.D. in computer science from Zhejiang University, now is an associate professor at Columbia University College of Surgeon and Surgery and a senior research scientist at New York State Psychiatric Institute. His research interest includes biomedical image processing and analysis, virtual reality technology in brain function research, and scientific visualization.

References

[1]. Basser PJ, Mattiello J, LeBihan D. MR diffusion tensor spectroscopy and imaging. Biophys J. 1994; 66(1):259–67. [PubMed: 8130344]

[2]. Wu EX, Cheung MM. MR diffusion kurtosis imaging for neural tissue characterization. NMR Biomed. 2010; 23(7):836–48. [PubMed: 20623793]

[3]. Veraart J, Poot DH, Van Hecke W, Blockx I, Van der Linden A, Verhoye M, et al. More accurate estimation of diffusion tensor parameters using diffusion Kurtosis imaging. Magn Reson Med. 2011; 65(1):138–45. [PubMed: 20878760]

[4]. Jensen JH, Helpern JA, Ramani A, Lu H, Kaczynski K. Diffusional kurtosis imaging: the quantification of non-Gaussian water diffusion by means of magnetic resonance imaging. Magn Reson Med. 2005; 53(6):1432–40. [PubMed: 15906300]

[5]. Lu H, Jensen JH, Ramani A, Helpern JA. Three-dimensional characterization of non-Gaussian water diffusion in humans using diffusion kurtosis imaging. NMR Biomed. 2006; 19(2):236–47. [PubMed: 16521095]

[6]. Hui ES, Cheung MM, Qi L, Wu EX. Towards better MR characterization of neural tissues using directional diffusion kurtosis analysis. Neuroimage. 2008; 42(1):122–34. [PubMed: 18524628]

[7]. Lazar M, Jensen JH, Xuan L, Helpern JA. Estimation of the orientation distribution function from diffusional kurtosis imaging. Magn Reson Med. 2008; 60(4):774–81. [PubMed: 18816827]

[8]. Jensen JH, Helpern JA. MRI quantification of non-Gaussian water diffusion by kurtosis analysis. NMR Biomed. 2010; 23(7):698–710. [PubMed: 20632416]

[9]. Raab P, Hattingen E, Franz K, Zanella FE, Lanfermann H. Cerebral gliomas: diffusional kurtosis imaging analysis of microstructural differences. Radiology. 2010; 254(3):876–81. [PubMed: 20089718]

[10]. Falangola MF, Jensen JH, Babb JS, Hu C, Castellanos FX, Di Martino A, et al. Age-related non-Gaussian diffusion patterns in the prefrontal brain. J Magn Reson Imaging. 2008; 28(6):1345–50. [PubMed: 19025941]

[11]. Helpern JA, Adisetiyo V, Falangola MF, Hu C, Di Martino A, Williams K, et al. Preliminary evidence of altered gray and white matter microstructural development in the frontal lobe of adolescents with attention-deficit hyperactivity disorder: a diffusional kurtosis imaging study. J Magn Reson Imaging. 2011; 33(1):17–23. [PubMed: 21182116]

[12]. Cheung MM, Hui ES, Chan KC, Helpern JA, Qi L, Wu EX. Does diffusion kurtosis imaging lead to better neural tissue characterization? A rodent brain maturation study. Neuroimage. 2009; 45(2):386–92. [PubMed: 19150655]

[13]. Wang JJ, Lin WY, Lu CS, Weng YH, Ng SH, Wang CH, et al. Parkinson disease: diagnostic utility of diffusion kurtosis imaging. Radiology. 2011; 261(1):210–7. [PubMed: 21771952]

[14]. Zhuo J, Xu S, Proctor JL, Mullins RJ, Simon JZ, Fiskum G, et al. Diffusion kurtosis as an in vivo imaging marker for reactive astrogliosis in traumatic brain injury. Neuroimage. 2012; 59(1):467–77. [PubMed: 21835250]

[15]. Peled S, Whalen S, Jolesz FA, Golby AJ. High *b*-value apparent diffusion-weighted images from CURVE-ball DTI. J Magn Reson Imaging. 2009; 30(1):243–8. [PubMed: 19557743]

[16]. Jensen, JH.; Hu, C.; Helpern, JA. Rapid data acquisition and post-processing for diffusional kurtosis imaging. Proceedings of the 17th scientific meeting; 2009. p. 1403

[17]. Poot DH, den Dekker AJ, Achten E, Verhoye M, Sijbers J. Optimal experimental design for diffusion kurtosis imaging. IEEE Trans Med Imaging. 2010; 29(3):819–29. [PubMed: 20199917]

[18]. Tabesh A, Jensen JH, Ardekani BA, Helpern JA. Estimation of tensors and tensor-derived measures in diffusional kurtosis imaging. Magn Reson Med. 2011; 65(3):823–36. [PubMed: 21337412]

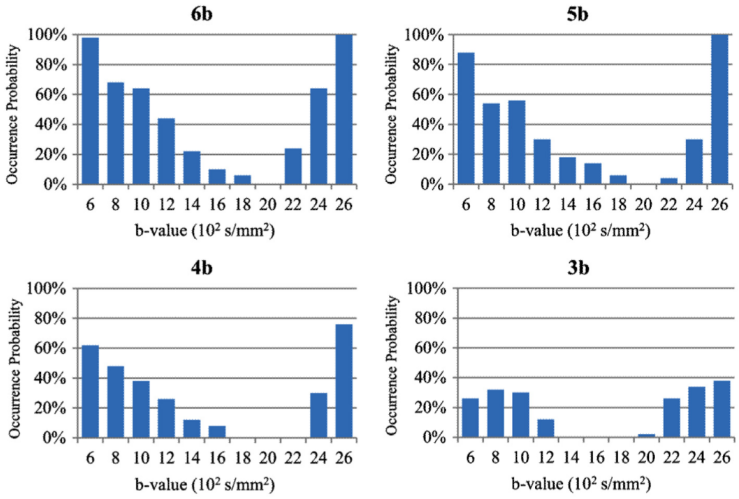

Fig. 1.

The occurrence probability of each nonzero *b*-value in the highest 10 ranked (top 10) schemas that we identified as *high-performance* based on the root mean square error (RMSE) calculated for 3–6 *b*-value (3b, 4b, 5b and 6b, respectively) cases. We constructed all potential DKI datasets acquired at 3b to 6b schemas by extracting DWI data from a dataset of 12 *b*-values, and then estimating their corresponding ADC and AKC maps using the DKI model. Subsequently, we sorted the schemas based on the RMSE of their parameter maps and recorded the occurrence probability of every *b*-value in the top 10 schemas for 3b to 6b cases, respectively. The results showed that *b*-values at the two end positions of the *b*-value range had significantly large contributions to these top 10 schemas. We inferred that the schemas can be optimized by acquiring DWI data with *b*-values scattered to the two ends of the *b*-value range (600–1200 and 2400–2600 s/mm^2). These *b*-values had higher occurrence probability (52% on average) than those in the middle of the range, especially those values within the 1600–2000 s/mm^2 range (occurrence probability = 4% on average).

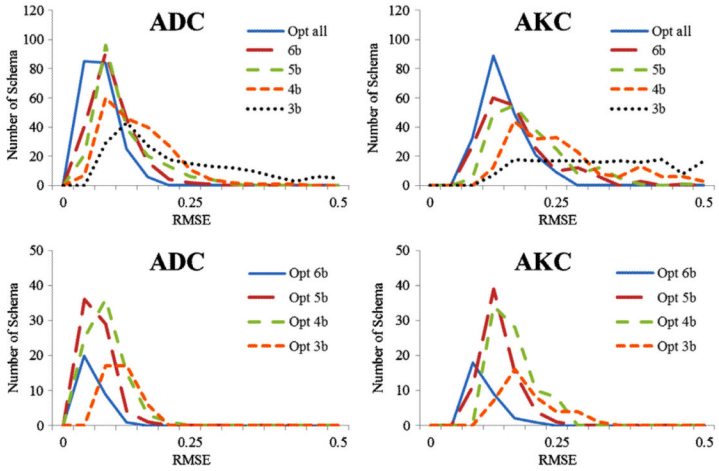

Fig. 2.

Bootstrap analysis of the RMSE distribution based on the 5 types of acquisition schemas. We compared the RMSE distributions of 5 schema groups. The first row: The result of group 1 containing all schemas that satisfied the high-performance criterion (Fig. 1) including 3b to 6b schemas is shown as blue line; The results of group 2–5, i.e., schemas containing 3–6 *b*-values, respectively, are shown as the other 4 types of lines. The second row shows RMSE distributions of high-performance schemas with 3–6 *b*-values, respectively, which employed all schemas instead of using a bootstrapping strategy because the numbers of these schemas were limited. The results showed that the RMSE distribution gradually widened from the 6b to the 3b case; the mean RMSE and standard deviation of MD and MK increased from 0.09 ± 0.04, 0.16 ± 0.07 to 0.24 ± 0.16, 0.37 ± 0.16. While the high-performance schemas (across all of the 3b to 6b cases) minimized the estimation error, and generated RMSE within a narrow region in the lower end of the RMSE value range (0.07 ± 0.03 for MD and 0.14 ± 0.04 for MK).

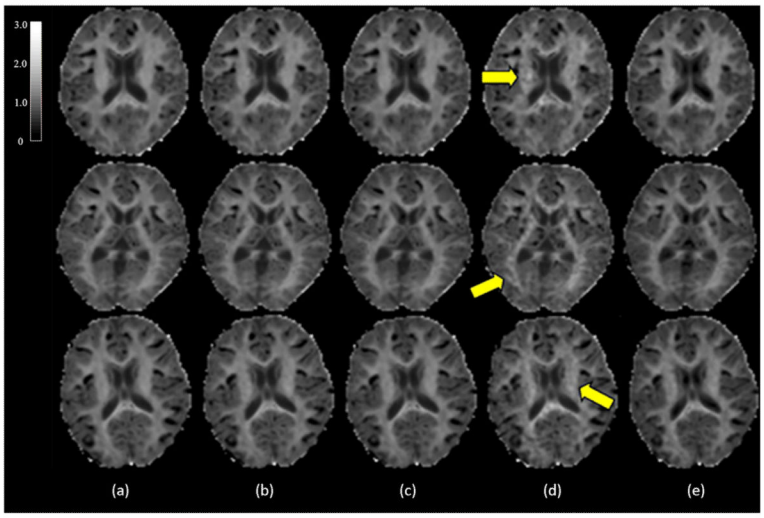

Fig. 3.

Comparison of the MK maps using conventional acquisition schemas with equally spaced *b*-values (ESB) and our optimized schemas. We used the optimized schemas of 3b and 6b according to the previous statistics (OPT 3b and OPT 6b in Table 1). From left to right: ground truth (a), MK maps of ESB 6b (b), OPT 6b (c), ESB 3b (d) and OPT 3b (e). The MK maps were generated from data collected from 3 participants. The results showed that both ESB and the optimized schemas can produce accurate MK maps using 6 *b*-values. However, the ESB 3b schema generated artifacts (yellow arrows in (d)), whereas the OPT 3b schema did not. (For interpretation of the references to color in text, the reader is referred to the web version of this article.)

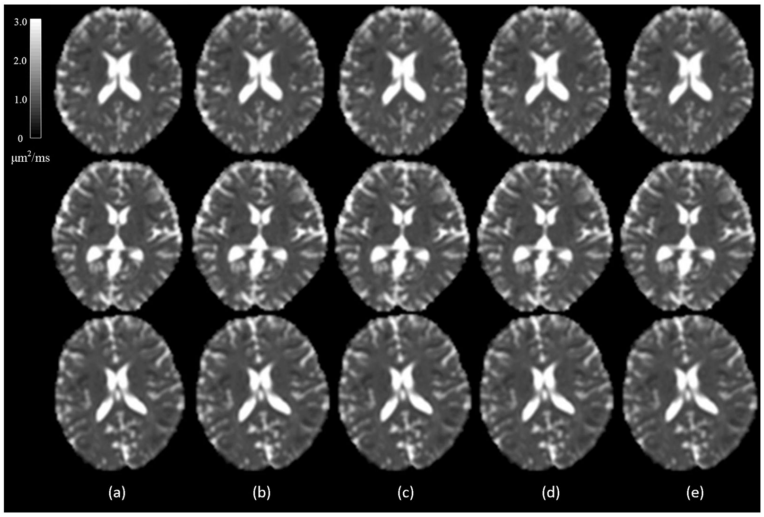

Fig. 4.
Comparison of MD maps using the conventional ESB and optimized schemas. From left to right: ground truth (a), MD maps of ESB 6b (b), OPT 6b (c), ESB 3b (d), and OPT 3b (e).

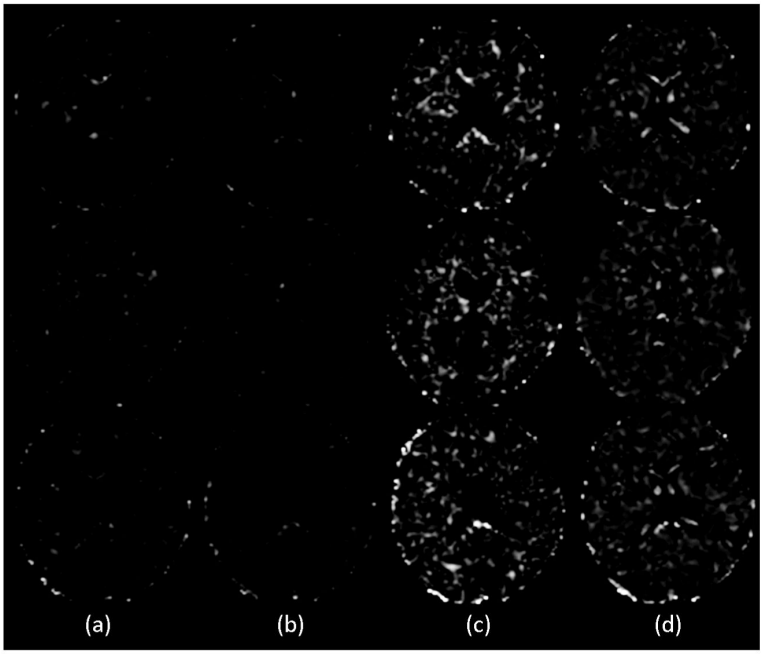

Fig. 5.

Residual maps of MK maps. From left to right: Residual map of the MK maps estimated using ESB 6b (a), OPT 6b (b), ESB 3b(c) and OPT 3b (d). The optimized schemas (b and d) outperformed their counterparts (a and c) with less residuals and the OPT 6b schema performed the best in that it contained the fewest residuals. Note that brightness and contrast were enhanced for better visualization.

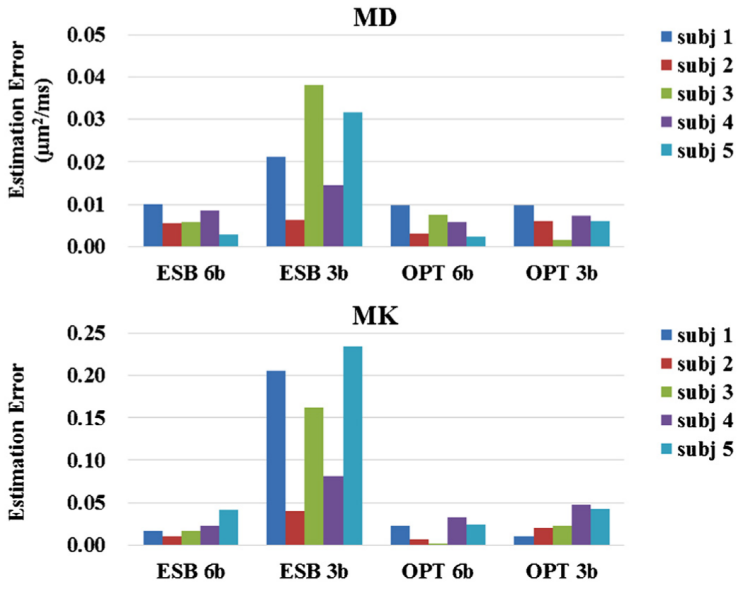

Fig. 6.

ROI comparison of the ESB and OPT schemas. An ROI was manually drawn for each participant in regions identified as sensitive to different schemas according to the visual test. Estimation error of mean MD and MK in these ROIs were calculated and compared. The ESB3b performed the worst and the performance of the OPT 3b schemas were very similar to that of the 6b schemas.

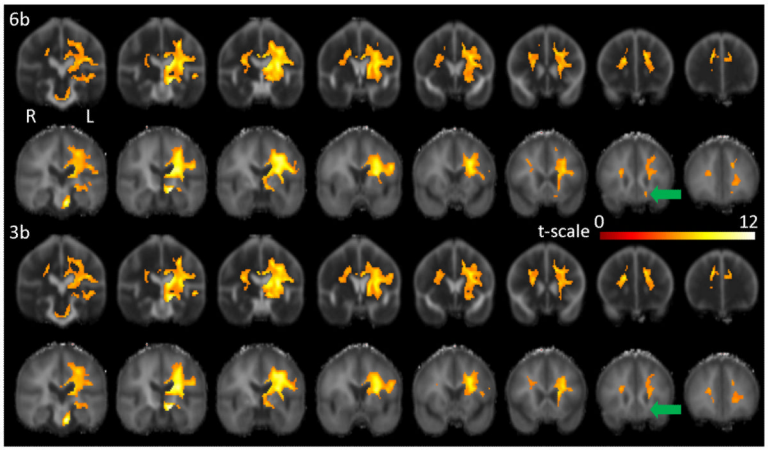

Fig. 7.

Voxel-based analysis (VBA) between healthy controls and right-side stroke patients. The results of the two-sample *t*-test of MD and MK were respectively superimposed onto the averaged MD and MK maps of all subjects using Xjview (http://www.alivelearn.net/xjview8). Two DKI acquisition schemas were tested: the ESB 6b schema with *b*-values from 0 to 2500 s/mm^2 (upper 2 rows) and the OPT 3b schema with *b*-value at 0, 1000 and 2500 s/mm^2 (lower 2 rows). The first and third rows are MD and the second and fourth rows are MK maps. Significantly reduced MK values and increased MD values were visible in the stroke patient group. The two schemas produced very similar results, except for some minor differences (see green arrow). (For interpretation of the references to color in text, the reader is referred to the web version of this article.)

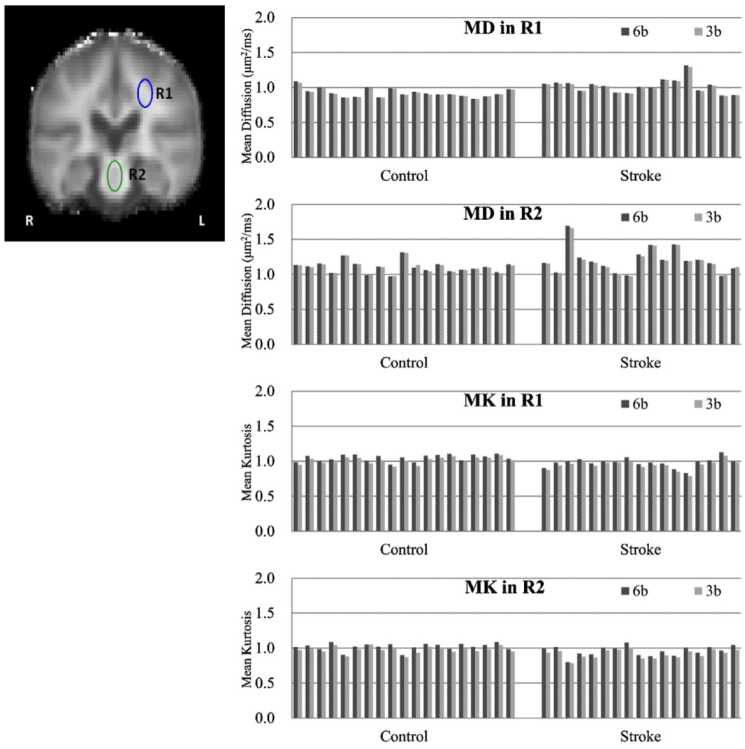

Fig. 8.

Mean MD and MK values in two ROIs in the corona radiata (R1) and brainstem (R2). We calculated the mean MD (rows 1 and 2) and MK (rows 3 and 4) values in these ROIs for all 36 participants (19 controls and 17 stroke patients). The results showed that the 6b ESB schema and 3b optimized schema yielded similar parameter values in both ROIs for every participant. (The horizontal axis in these figures reflects either the 19 controls or the 17 stroke patients.)

Table 1

The *b*-value list of the equally spaced *b*-value (ESB) schemas and the optimized (OPT) schemas with 3–6 *b*-values. We calculated the RMSE of ADC and AKC. The results showed that the OPT schemas (those with the highest averaged ranking in our experiments) outperformed the conventional ESB schemas in all *b*-value cases, with approximately 14%/24% less RMSE for ADC/AKC in 4b to 6b cases and up to 31%/44% less RMSE in the 3b case (in bold). Moreover, as the number of *b*-values involved in the schemas decreased, increases in the RMSE of the optimal schemas was slower and more stable than that of ESB schemas, with decreasing ratios at 91% and 85% (OPT) versus 133% and 152% (ESB). Thus, reducing the number of *b*-values is a feasible solution to reduce the DKI acquisition time with a slight loss of accuracy.

	b List	ADC RMSE	AKC RMSE
ESB 6b	0 600 1000 1600 2000 2600	0.0454	0.1064
ESB 5b	0 800 1400 2000 2600	0.0613	0.1331
ESB 4b	0 800 1600 2600	0.0672	0.1476
ESB 3b	0 1000 2000	0.1058	**0.2686**
OPT 6b	0 600 1000 1200 2400 2600	0.0383	0.0818
OPT 5b	0 600 1200 2400 2600	0.0622	0.1059
OPT 4b	0 600 1200 2600	0.0628	0.1322
OPT 3b	0 800 2600	0.0733	**0.1511**

Table 2

Regions showing significant increases in MD and decreases in MK for the stroke patient group compared to the healthy control group. The differences in cluster size of these regions were below 7%.

		Hemisphere	Cluster size	Peak *t* value	MNI coordinate		
					x	*y*	*z*
MD↑	ESB 6b	Left	6772	10.6569	−26	−6	12
		Right	1035	7.7995	18	26	21
	OPT 3b	Left	6901	10.9958	−26	−6	12
		Right	1108	7.9780	18	26	21
MK↓	ESB 6b	Left	6165	11.2663	−14	−14	−9
		Right	192	6.4460	24	22	18
	OPT 3b	Left	5774	11.4016	−12	−16	−12
		Right	192	6.2864	22	26	18

Peak coordinates represent the location of the maximum t value in MNI space (Montreal Neurological Institute 152). $P < 0.00001$ (uncorrected) and cluster size > 100 pixels.